Experimental investigations and phase-field simulations of triple-phase-separation kinetics within liquid ternary Co-Cu-Pb immiscible alloys

Y. H. Wu, W. L. Wang, N. Yan, and B. Wei*

Department of Applied and Physics, Northwestern Polytechnical University, Xi'an 710072, People's Republic of China

(Received 7 November 2016; revised manuscript received 31 March 2017; published 8 May 2017)

The phase-separation kinetics and microstructure evolution mechanisms of liquid ternary $Co_{43}Cu_{40}Pb_{17}$ immiscible alloys are investigated by both the drop tube technique and phase-field method. Two successive phase separations take place during droplet falling and lead to the formation of a three-phase three-layer core-shell structure composed of a Co-rich core, a Cu-rich middle layer, and a Pb-rich shell. The Pb-rich shell becomes more and more conspicuous as droplet diameter decreases. Meanwhile, the Co-rich core center gradually moves away from the core-shell center. Theoretical analyses show that a larger temperature gradient inside a smaller alloy droplet induces the accelerated growth of the surface segregation shell during triple-phase separation. The residual Stokes motion and the asymmetric Marangoni convection result in the appearance of an eccentric Co-rich core and the core deviation degree is closely related to the droplet size and initial velocity. A three-dimensional phase-field model of ternary immiscible alloys, which considers the successive phase separations under the combined effects of Marangoni convection and surface segregation, is proposed to explore the formation mechanisms of three-phase core-shell structures. The simulated core-shell morphologies are consistent with the experimental observations, which verifies the model's validity in reproducing the core-shell dynamic evolution. Numerical results reveal that the development of three-phase three-layer core-shell structures can be attributed to the primary and then secondary phase separations dominated simultaneously by Marangoni convection and surface segregation. Furthermore, the effects of droplet temperature gradient on the growth kinetics of the surface segregation shell are analyzed in the light of phase-field theory.

DOI: 10.1103/PhysRevE.95.052111

I. INTRODUCTION

Liquid phase separation (PS) inside small droplets of immiscible alloys often leads to the formation of core-shell microstructures [1–3] under the drop tube [3], aerodynamic levitation [4], and gas atomization [5] conditions. Due to their various potential applications in the areas of condensed matter physics and material sciences, these core-shell microstructures have attracted much attention in recent years. The formation mechanisms and evolution processes of core-shell microstructures in small droplets of undercooled liquid immiscible alloys have been investigated extensively. When the immiscible alloy is undercooled into the miscibility gap, the minority liquid phase is separated from the parent liquid phase in the form of tiny globules. The subsequent growth and movement of these globules in the process of PS are determined by many factors, including Marangoni motion [6], Brownian motion [7], Ostwald ripening [8,9], convection flow [10], gravity level [3], and wettability between the two-coexisting phases [11]. In microgravity, Stokes sedimentation caused by the density difference between the two-coexisting liquid phases is greatly weakened and Marangoni convection becomes the dominant dynamic mechanism responsible for the development of core-shell microstructures. Under the effect of Marangoni convection, the minor phase globules migrate from the lower-temperature regions to the higher-temperature regions [12] at the droplet center, forming a core, and the other phase is pushed outside, forming a shell. This is qualified as an interpretation of the formation of two-layer core-shell structures [13], but fails to explain the development of core-shell structures with more than two layers. After these structures were intensively studied, it was found that surface segregation, which is induced by the surface energy difference between the two-coexisting liquids, is the other dynamic mechanism responsible for the formation of core-shell structures [3].

Most of the previous investigations on the liquid PS inside tiny droplets of immiscible alloys have concentrated on two-phase core-shell microstructures, which correspond to core-shell structures composed of *A*- and *B*-rich immiscible zones [14,15]. In contrast, the three-phase core-shell microstructures, which represent core-shell structures consisting of *A*-, *B*-, and *C*-rich immiscible zones, have rarely been involved so far. The formation of three-phase immiscible zones requires a cascade of PSs in undercooled melts of multicomponent immiscible alloys. The preparation of a three-phase core-shell structure via liquid PS remains a great challenge, let alone its formation mechanisms and evolution processes. Due to the ultrashort solidification time and the opacity of liquid immiscible alloys, it is very difficult to directly monitor the evolution processes of various core-shell structures, which are currently studied based on metallographic analysis [16]. The dynamic mechanisms and evolution processes are not fully understood, especially for the three-phase core-shell structures. Until now, the numerical simulations have been widely applied in the theoretical research of liquid PS [17–23], but they mainly focus on organic mixtures [17,18] and polymers [20,21]. There is still much work to be done on these core-shell structures in undercooled liquid immiscible alloys. However, few theoretical models have been proposed to investigate the evolution kinetics of three-phase core-shell structures during the successive liquid PSs. Therefore, it

*Corresponding author: bbwei@nwpu.edu.cn

is of great importance to investigate a cascade of PSs in multicomponent immiscible alloys by both experiments and simulations.

The aim of this work is to prepare a three-phase core-shell structure via PS. In addition, the present paper is also devoted to modeling the dynamic evolution of this core-shell structure. In contrast with other containerless processing techniques, the drop tube method is characterized by subdividing liquid immiscible alloys into numerous droplets at a reduced-gravity state. It may be a preferable choice to produce the spherical composites with various core-shell structures. The ternary $Co_{43}Cu_{40}Pb_{17}$ immiscible alloy, which perhaps displays successive phase separations of $L \rightarrow L_1$(Co-rich) + L_2(Cu-rich) and L_2(Cu-rich) $\rightarrow$ $L_{2''}$(Cu-rich) + L_3(Pb-rich), is selected to tentatively synthesize the core-shell structure consisting of Co-, Cu-, and Pb-rich immiscible zones by performing drop tube experiments. To sufficiently clarify the formation mechanisms of three-phase core-shell structures, a three-dimensional phase-field model is proposed to analyze the dynamical evolution characteristics of liquid PS in undercooled melts of ternary Co-Cu-Pb alloys. The model takes into account the successive PSs under the coupling effects of Marangoni convection and surface segregation. Based on this model, the phase separation and microstructure evolution of Co-Cu-Pb alloy droplets under reduced-gravity condition are systematically explored in subsequent sections.

II. EXPERIMENTAL PROCEDURE

The experimental samples of the ternary $Co_{43}Cu_{40}Pb_{17}$ alloy were made from high-purity elements of 99.99% Co, 99.99% Cu, and 99.99% Pb in a high-vacuum arc-melting furnace. Each sample weighed about 3 g and was placed inside a $\Phi 16 \times 150$ mm^2 quartz tube with a small orifice about 0.3 mm in diameter at the bottom. The quartz tube was subsequently installed on the top of the drop tube equipment. Before the experiment, the drop tube was evacuated to 2×10^{-5} Pa and then backfilled with a mixture of He (99.995%) and Ar (99.999%) gas to 1×10^5 Pa. The partial pressure ratio of Ar gas to He gas was 1:1. After that, the alloy sample was melted by induction heating and further overheated to 100–300 K above its liquidus temperature for a few seconds. Finally, the molten alloy was ejected out from the orifice and dispersed into many droplets by high-pressure jetting gas of He, which fell and solidified in a containerless and reduced-gravity environment.

The solidified droplets were collected at the bottom of the drop tube. Later on, they were classified into different groups according to droplet size. Afterward, these solidified droplets were mounted, polished, and etched. A solution of 5 g of $FeCl_3$ + 10 mL of HCl + 50 mL of H_2O was used as the etchant for ternary Co-Cu-Pb alloys. The solidified microstructures were investigated with an FEI Sirion Electron Microscope and a Zeiss Axiovert 200 MAT optical microscope. The solute contents of Co-, Cu-, and Pb-rich immiscible zones were finally measured by an INCA Energy 300 energy dispersive spectrometer (EDS).

III. THREE-DIMENSIONAL PHASE-FIELD SIMULATIONS

A. Free energy functional construction

In this model, a ternary immiscible alloy comprised of components A, B, and C is considered. For simplification, the molecular weights, specific volumes, and viscosities of A, B, and C elements within the ternary A-B-C alloy are supposed to be equal. In such a case, the molar, volumetric, and mass fractions are all equal to each other and the mixture viscosity is composition independent [24–26]. As for the Co-Cu-Pb alloy, this supposition does not apply in the presence of Pb. Considering the present work is devoted to the exploration of formation mechanisms of three-phase core-shell structures in microgravity, our model based on this supposition still can be used to qualitatively study the evolution kinetics of the three-phase core-shell structure during triple-phase separation. Let $C_i(\mathbf{r},\tau)$ for $i = 1,2$, and 3 represent the mole concentrations of the components Co, Pb, and Cu as functions of $\mathbf{r}$ and τ, respectively. Here $\mathbf{r}$ denotes the spatial position and τ stands for the evolution time. According to the mass conservation, the mole concentrations satisfy

$$\sum_{i=1}^{3} C_i(\mathbf{r},\tau) = 1. \tag{1}$$

The free energy functional for a ternary immiscible alloy droplet can be expressed as

$$F_{\text{total}}(\mathbf{r},\tau) = F_{\text{bulk}}(\mathbf{r},\tau) + F_{\text{grad}}(\mathbf{r},\tau) + F_{\text{surface}}(\mathbf{r},\tau), \tag{2}$$

where F_{bulk} is the bulk free energy, F_{grad} is the free energy of the concentration gradient, and F_{surface} is the surface free energy. With use of a regular solution model [27,28], the bulk free energy F_{bulk} can be simulated as

$$F_{\text{bulk}}(\mathbf{r},\tau) = \int \left(\sum_{i \neq j} \sigma_{ij} C_i C_j + \sum_{i=1}^{3} C_i \ln C_i \right) (R_g T) dV, \tag{3}$$

$$\sigma_{ij} = \frac{\omega_{ij}}{R_g T}, \tag{4}$$

where ω_{ij} is the effective interaction energy between components i and j, R_g is the gas constant, and T is the temperature of the alloy melt. In the present work the values of σ_{12}, σ_{13}, and σ_{23} are supposed to be the same σ for simplification. Furthermore, the values of ω_{12}, ω_{13}, and ω_{23} are set as $R_g T_c \Omega$ and Ω is the interaction coefficient. If $\sigma \geqslant 3$, F_{bulk} has three minima and one local maximum. This energy allows for one-, two-, and three-phase materials. The free energy F_{grad} of the concentration gradient [29] and the surface free energy [13] F_{surface} are taken, respectively, as

$$F_{\text{grad}}(\mathbf{r},\tau) = \int \sum_{i=1}^{3} 0.5 R_g T_c a_s^2 (\nabla C_i)^2 dV, \tag{5}$$

$$F_{\text{surface}}(\mathbf{r},\tau) = \sum_{i=1}^{3} \left(F_i - H C_{S-i} + 0.5 g_S C_{S-i}^2 \right) (R_g T_c) S_i, \tag{6}$$

in which C_{S-i} represents the mole concentration of component i at the surface and S_i determines the surface segregation. Here S_i is set as 1 for the component i with the lowest surface energy and as 0 for other components. In addition, T_c is the critical temperature, a_s is the characteristic length of spatial heterogeneity, and F_i, H, and g_S are constants describing the surface preferential attraction properties. The dimensionless chemical potential μ_i of component i in the alloy melt is derived as

$$\mu_i = \frac{1}{R_g T_c}\frac{\delta F_{\text{total}}}{\delta C_i} = \frac{1}{R_g T_c}\left(\frac{\partial F_{\text{total}}}{\partial C_i} - \nabla\frac{\partial F_{\text{total}}}{\partial \nabla C_i}\right). \quad (7)$$

B. Concentration-field governing equation

According to the model in Refs. [25,26], the dimensional concentration-field governing equation for component i in the process of PS can be determined as

$$\frac{\partial C_i}{\partial \tau} = \nabla\cdot\left\{C_i\left[-\mathbf{v} + \sum_{j\neq i} C_j \nabla\left(\frac{\delta F}{\delta C_i} - \frac{\delta F}{\delta C_j}\right)\right]\right\}, \quad (8)$$

where $\mathbf{v}$ is the velocity. Since the equilibrium is defined via equal chemical-potential gradients, the elements of the transport matrix for diffusion should sum to zero in each row and of course in each column to guarantee $C_1 + C_2 + C_3 = 1$. To avoid the problems of labeling the variables, we first define a transport matrix for diffusion with respect to C_1, C_2, and C_3 and then calculate the chemical potential with Eq. (7). Subsequently, we use them in the equation (8) of motion. As for a tiny droplet, it has been proved that the Reynolds number is smaller than 10^{-3} and the local velocity $\mathbf{v}$ of the inner flow field is proportional to the local body force [30,31]. As the local body force approximation is taken into account, the velocity $\mathbf{v}$ can be simplified as

$$\mathbf{v}(\mathbf{r},\tau) \approx -P_F \sum_{i=1}^{3} C_i \nabla \mu_i, \quad (9)$$

where P_F is the fluidity parameter of the alloy melt. It can be defined as

$$P_F = \frac{\rho R_g T_c \varepsilon^2}{6\pi D_L \eta M}, \quad (10)$$

where ρ is the density of the alloy droplet, η is the viscosity, D_L is the solute diffusion coefficient, and M is the molar weight. Here Eq. (8) refers to an incompressible system. To satisfy the incompressibility condition of $\nabla\cdot\mathbf{v} = 0$, a Lagrange multiplier must be introduced in the local body force approximation [25,26], yielding

$$\mathbf{v}(\mathbf{r},\tau) \approx -P_F\left[-\nabla\theta(\mathbf{r},\tau) + \sum_{i=1}^{3} C_i \nabla\mu_i\right], \quad (11)$$

$$\nabla\cdot\mathbf{v} = 0. \quad (12)$$

Based on Eqs. (11) and (12), $\theta(\mathbf{r},\tau)$ can be obtained by solving the following equation:

$$\nabla^2\theta(\mathbf{r},\tau) = \sum_{i=1}^{3} \nabla\cdot(C_i\nabla\mu_i). \quad (13)$$

C. Temperature-field governing equation

Under the reduced-gravity condition, the effects of Stokes sedimentation on the migration of minor phase globules can be greatly weakened and the Marangoni convection caused by the temperature gradient starts to dominate the globule movement during PS. To incorporate the effects of Marangoni convection on liquid PS, a dimensionless heat conduction equation [3]

$$\frac{\partial T_r}{\partial \tau} = \frac{\alpha_T}{D_L}\left(\frac{\partial^2 T_r}{\partial r^2} + \frac{2}{r}\frac{\partial T_r}{\partial r}\right) \quad (14)$$

is adopted, where $T_r = T/T_c$ is the reduced temperature and α_T and D_L are the thermal and solutal diffusion coefficients, respectively. The initial and boundary conditions for Eq. (14) are given as

$$T(\mathbf{r},0) = T_0, \quad (15)$$

$$-k\left.\frac{\partial T}{\partial r}\right|_{r=R} = \varepsilon_h\sigma_{\text{SB}}\left({T_s}^4 - {T_g}^4\right) + h(T_s - T_g), \quad (16)$$

where k is the thermal conductivity, ε_h is the emissivity, σ_{SB} is the Stefan-Boltzmann constant, h is the heat transfer coefficient, T_0 is the initial temperature of the alloy melt, T_g is the environment temperature, and T_s is the surface temperature of the alloy droplet. Although Eqs. (14)–(16) roughly describe the droplet heat dissipation prior to liquid PS and possible effects from PS and fluid flow inside the small droplets are ignored, the simulated temperature fields are still helpful to understand the formation mechanisms of multiphase core-shell structures for immiscible alloy droplets processed by the drop tube method [13].

D. Model solutions

The governing equations of this three-dimensional (3D) phase-field model were solved on a uniform three-dimensional cubic grid by using an explicit finite-difference method and zero Neumann boundary conditions for C_i and μ_i were imposed at the boundaries. The system size used in the simulations was chosen as $140\Delta x \times 140\Delta y \times 140\Delta z$, with $\Delta x = \Delta y = \Delta z = 1$. The droplet diameter was supposed to be $120\Delta x$ and Δt was taken as 0.0002, which ensures the stability of the numerical solutions. During the calculations, we considered that the diffusion flux should vanish at vanishing field, i.e., $\mathbf{q}_i|_{C_i=0} = 0$ is a basic requirement to avoid dynamic spurious phases. The values of the physical parameters in this model were obtained from Ref. [32]. The codes used to solve the phase-field model were written in C++ language and the calculations were carried out by a Lenovo 1800 cluster system.

IV. RESULTS AND DISCUSSION

A. Triple-phase separation under reduced-gravity state

In the drop tube experiment, the liquid ternary $Co_{43}Co_{40}Pb_{17}$ alloy is rapidly solidified in the form of numerous small droplets with different sizes. While droplets fall, two successive PSs take place and finally result in the formation of two kinds of three-layer core-shell structures as observed in Fig. 1. The EDS analyses reveal that the black denotes the Co-rich phase, gray represents the Cu-rich phase,

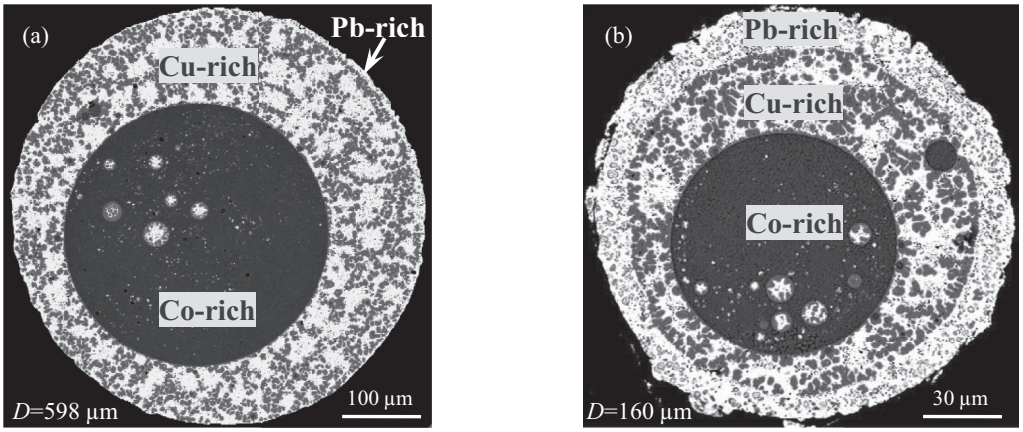

FIG. 1. Three-phase three-layer core-shell microstructures composed of a Co-rich core, a Cu-rich middle layer, and a Pb-rich shell in $Co_{43}Cu_{40}Pb_{17}$ alloy droplets solidified within the drop tube: (a) a thin Pb-rich shell and (b) a thick Pb-rich shell.

and white stands for the Pb-rich phase. Clearly, both core-shell structures are composed of a Co-rich core, a Cu-rich middle layer, and a Pb-rich shell. Furthermore, some Cu-rich globules appear within the Co-rich core. The only differences between these two core-shell structures are the reduced radius and the deviation degree of the Co-rich core and the reduced thicknesses of the Cu-rich layer and the Pb-rich shell. In the present work the reduced thickness δ_r of the Pb-rich shell, the reduced thickness L_r of the Cu-rich layer, the reduced radius R_r of the Co-rich core, and the deviation degree e_d of the Co-rich core are defined, respectively, as δ/R, L/R, r/R, and S/R in Fig. 2, where δ is the shell thickness, R is the droplet radius, L is the Cu-rich layer thickness, r is the average radius of the Co-rich core, and S is the distance between the Co-rich core center and the alloy droplet center.

According to the metallographic analyses, the morphology characteristics of three-phase three-layer core-shell structures are closely linked with alloy droplet diameter. Figure 2(a) shows the reduced thickness of the Pb-rich shell as a function of droplet diameter. It can be observed that the variation

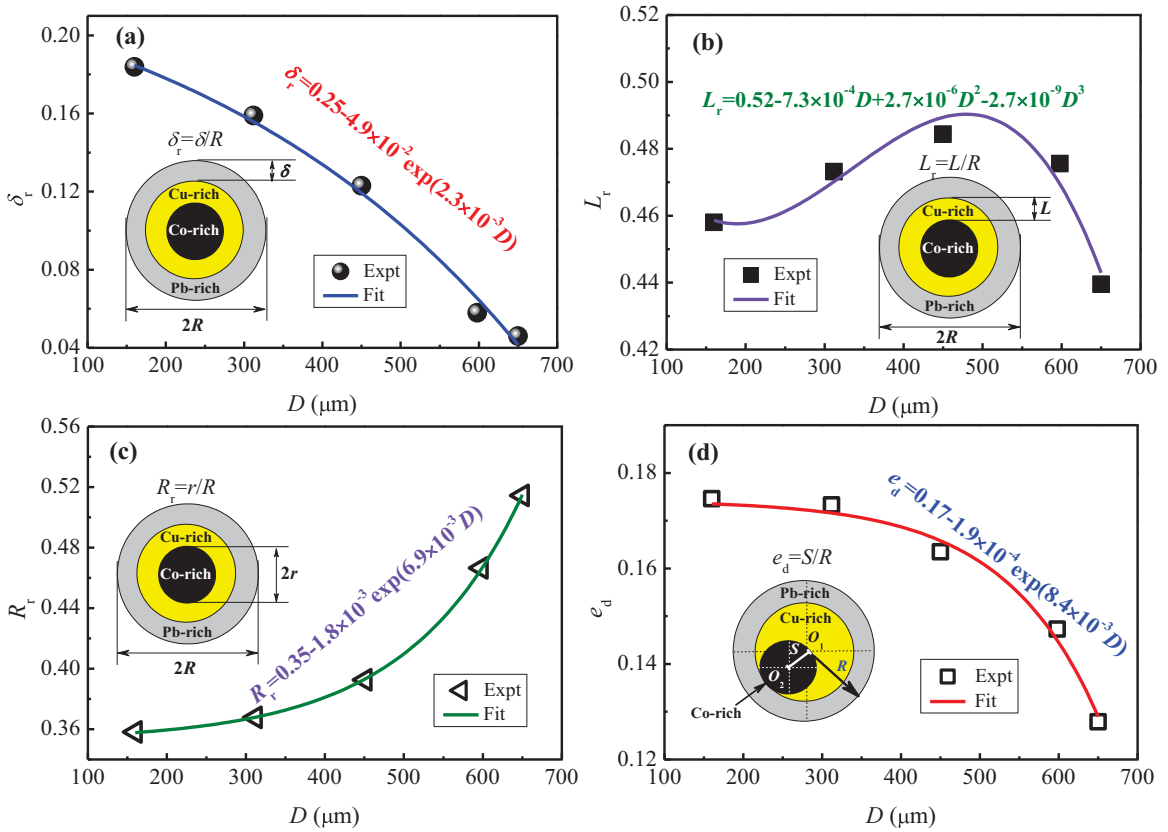

FIG. 2. Morphology characteristics of the three-phase three-layer core-shell structure versus alloy droplet size: (a) reduced thickness δ_r of the Pb-rich shell, (b) reduced thickness L_r of the Cu-rich layer, (c) reduced radius R_r of the Co-rich core, and (d) deviation degree e_d of the Co-rich core.

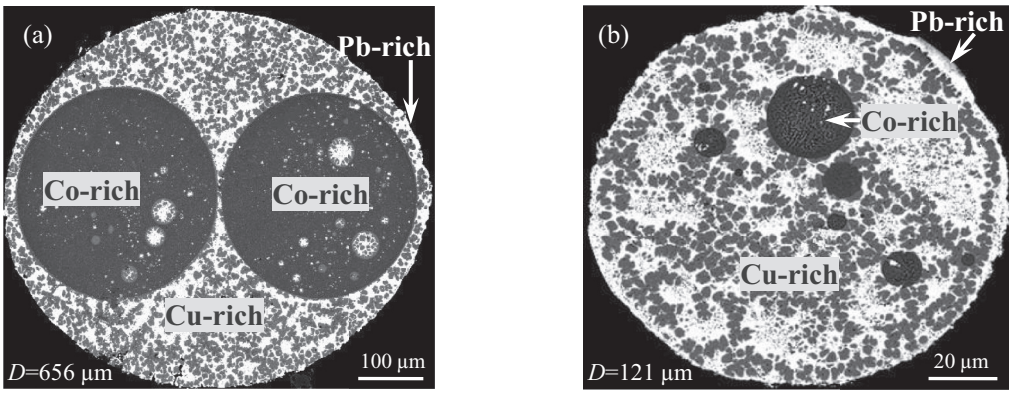

FIG. 3. Unusual three-phase separated morphologies of $Co_{43}Cu_{40}Pb_{17}$ alloy droplets under the drop tube condition: (a) multicore-shell structure and (b) dispersed structure.

of reduced thickness with droplet diameter could be fitted by an exponential relation. With decreasing droplet size, the reduced thickness increases slightly and this indicates that the Pb-rich shell becomes more and more obvious. Figure 2(b) illustrates the dependence of the reduced thickness of the Cu-rich middle layer on the alloy droplet diameter. As droplet size decreases, the reduced thickness of the Cu-rich layer displays an increasing trend in diameter regime above 500 μm. Once the droplet size decreases below this threshold value, the middle layer becomes narrower. In contrast, the reduced radius for the Co-rich core continually decreases with the drop in droplet diameter and the relationship between them can also be represented by an exponential function, as shown in Fig. 2(c). The deviation degree of the Co-rich core is also measured at various droplet sizes and the results are plotted in Fig. 2(d). Apparently, the core eccentric degree increases mildly with the decrease in droplet size. This suggests that the Co-rich core is gradually moving away from the core-shell center. It can be concluded that the droplet size plays an important role in the PS processes of $Co_{43}Cu_{40}Pb_{17}$ alloy droplets and subsequently influences the phase-separated morphologies to some extent.

Some unusual three-phase-separated morphologies, whose formation probabilities of ~7% are much smaller than the three-phase three-layer core-shell structures, are also preserved occasionally within the solidified alloy droplets as given in Fig. 3. As for an alloy droplet with a diameter of 656 μm, a dicaryon three-phase core-shell structure is formed and the morphology appears as two Co-rich cores surrounded by a Cu-rich middle layer and an inconspicuous Pb-rich shell, as depicted in Fig. 3(a). Not all of the triple-phase separation inside the drop tube leads to the formation of a core-shell macrosegregation structure. Figure 3(b) exhibits a dispersed three-phase-separated morphology consisting of Co-, Cu-, and Pb-rich zones. The evolution mechanisms of three-phase core-shell morphology characteristics with droplet size and the dominant factors responsible for the formation of these unusual macrosegregation patterns will be sufficiently discussed in the following.

B. Temperature-field characteristics

The formation of almost symmetrical three-layer core-shell microstructures in Fig. 1 can be attributed to the approximately symmetric temperature fields and concentration fields within falling Co-Cu-Pb alloy droplets. In the process of droplets falling, these alloy droplets are located in a containerless and reduced-gravity environment. Thus, the Stokes sedimentation caused by the density differences among coexisting liquids is greatly restrained and the Marangoni convection induced by the temperature gradient begins to control the movement of minor phase globules and then determines the final phase-separated morphology. Moreover, considering that the PS proceeds in a limited time related to the droplet cooling rate, developing a fundamental understanding of the temperature-field characteristics is highly desirable so as to clarify the dependent relation of phase-separated morphology on droplet size.

By using Eqs. (14)–(16), the variation of the droplet temperature T, temperature gradient G_L, and cooling rate R_c with the cooling time t can be calculated and the results are given in Fig. 4. For every alloy droplet, the closer to the droplet center, the higher the temperature, irrespective of droplet size, as shown in Fig. 4(a). As the interfacial energy between different coexisting liquids decreases with the rise in temperature, the minor phase globules during PS have a tendency to migrate to the droplet center with a higher temperature under the effect of Marangoni convection. In comparison to a large alloy droplet, the temperature of a small alloy droplet decreases more rapidly with the extension of cooling time, as illustrated in Fig. 4(b). In other word, a smaller alloy droplet has a higher cooling rate, as computed in Fig. 4(d). As a consequence, the larger alloy droplets may allow a longer migration time for these minor phase globules. In terms of Fig. 4(c), the temperature gradient of a smaller alloy droplet is significantly greater than that for alloy droplets with large sizes. Since the intensity of Marangoni convection is strongly dependent on the temperature gradient, it can be speculated that the Marangoni convection within a smaller droplet proceeds more intensely than that inside large droplets. Furthermore, the temperature gradient varies along the droplet radial direction. A high-temperature gradient appears at the droplet's outer regions, while the inner regions have a relatively small temperature gradient. This means that the intensity of Marangoni convection in regions near the alloy droplet surface is evidently stronger than that in regions around the droplet center. With extending the cooling time, the temperature

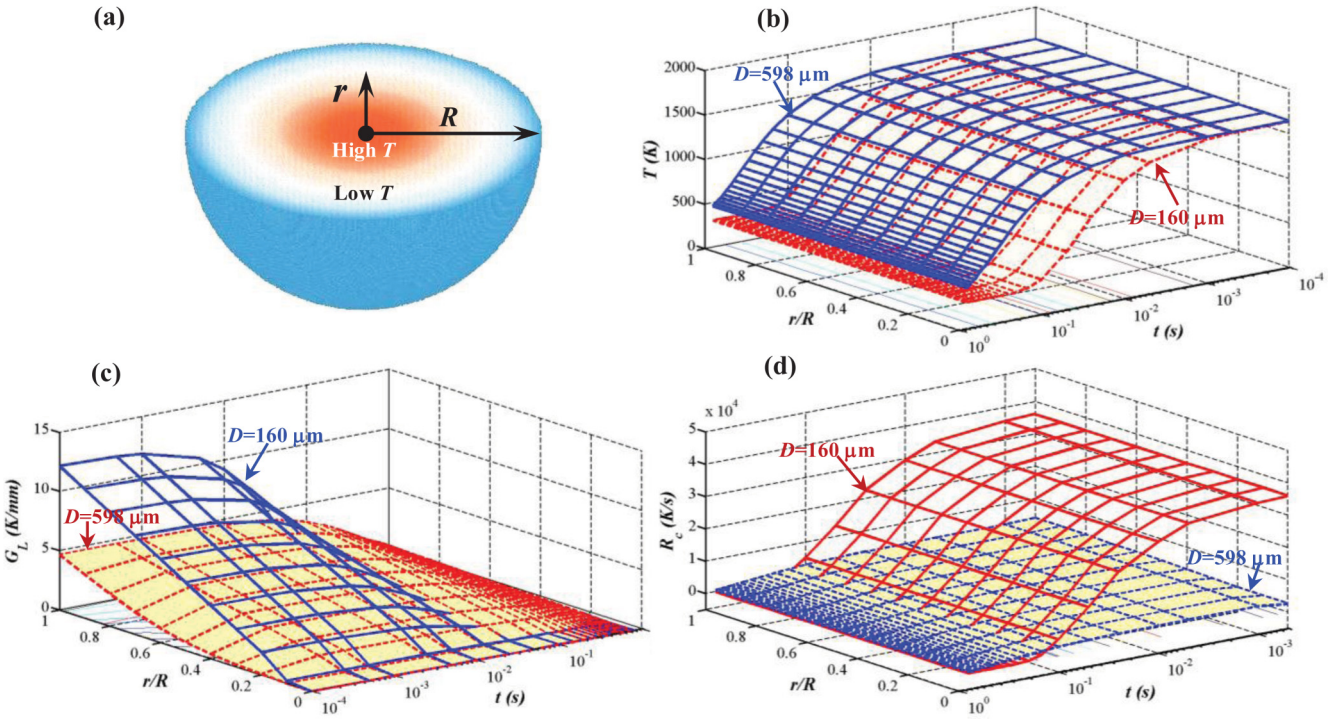

FIG. 4. Temperature-field profiles of $Co_{43}Cu_{40}Pb_{17}$ alloy droplets versus cooling time t and reduced radial distance r/R: (a) schematic diagram of the temperature field, (b) droplet temperature T-t-r/R, (c) temperature gradient G_L-t-r/R, and (d) cooling rate R_c-t-r/R.

gradient of every droplet decreases until reaching a value of zero. Apparently, the intensity of Marangoni convection is gradually weakened. The PS duration time is closely correlated with the droplet cooling rate. Because the heat dissipation of the droplet surface is more drastic than in the droplet interior, the droplet inner cooling rate is slightly lower than the droplet outer cooling rate, as observed in Fig. 4(d). Thus, the PS duration time is longer in the droplet's inner region than that around the droplet's periphery. In addition, it is also found that the variation of the droplet cooling rate with cooling time displays three stages. The cooling rate drops slowly in the first stage, beyond which it shows a rapidly reduction in the second stage. In the last stage, a dilatorily decrease occurs once again. The systematic understandings of temperature-field characteristics of ternary $Co_{43}Cu_{40}Pb_{17}$ alloy droplets contribute to the interpretation of the dynamic evolutions and formation mechanisms of three-phase three-layer core-shell structures.

As mentioned above, the reduced thickness δ_r of the surface segregation shell thickens with the decrease in droplet size. This is in good agreement with the phase-separated morphologies of Fe-Sn-Si immiscible alloy droplets inside a drop tube [33]. Why smaller droplets have a larger value of δ_r for the Pb-rich shell remains elusive so far. In view of phase-field simulations, the final phase-separated morphologies are mainly dominated by the PS time and the intensity of surface segregation and Marangoni convection. As is well known, the PS time is remarkably influenced by the droplet cooling rate and the intensity of Marangoni convection strongly depends on the temperature gradient. As given in Eqs. (2)–(7), the calculations of surface segregation for the Pb-rich liquid phase indirectly rely on the droplet temperature. Thus, a possible interpretation of the increasing thickness δ_r with the decrease of droplet size is the temperature-field difference between large and small droplets.

Here $Co_{43}Cu_{40}Pb_{17}$ alloy droplets with diameters of 598 and 160 μm in Fig. 1 are taken as examples to analyze the growth kinetics of the Pb-rich shell. As calculated in Fig. 4(c), the average temperature gradient inside a droplet with $D = 160\,\mu$m is far greater than that within a droplet at $D = 598\,\mu$m. It can be inferred that the smaller the droplet size the stronger the Marangoni convection. Due to the more intense Marangoni convection, the minor phase globules inside smaller droplets are easier to push inward to the droplet center during PS. As a result, more of the liquid phase of Co with the largest surface energy may migrate to the droplet center and coagulate to form a Co-rich core surrounded by a Cu-rich layer. At the same time, the chemical-potential gradient between the droplet surface and center increases remarkably for the Pb-rich liquid phase due to the enhanced temperature gradients of smaller droplets. In such a case, more and more of the liquid phase of Pb flows to the droplet surface in a shorter time and finally forms a thicker Pb-rich shell. According to the EDS analyses, with the decrease in droplet size, the Co content inside the Co-rich core increases while that of the Cu-rich middle layer presents the opposite variation. Meanwhile, the Pb content of the Co-rich core drops, whereas that within the Cu-rich middle layer rises. This is further proof that more liquid phases of Co and Pb are respectively impelled to aggregate together around the droplet center and surface because of the enhanced temperature gradient for those smaller alloy droplets. Therefore, a high-temperature

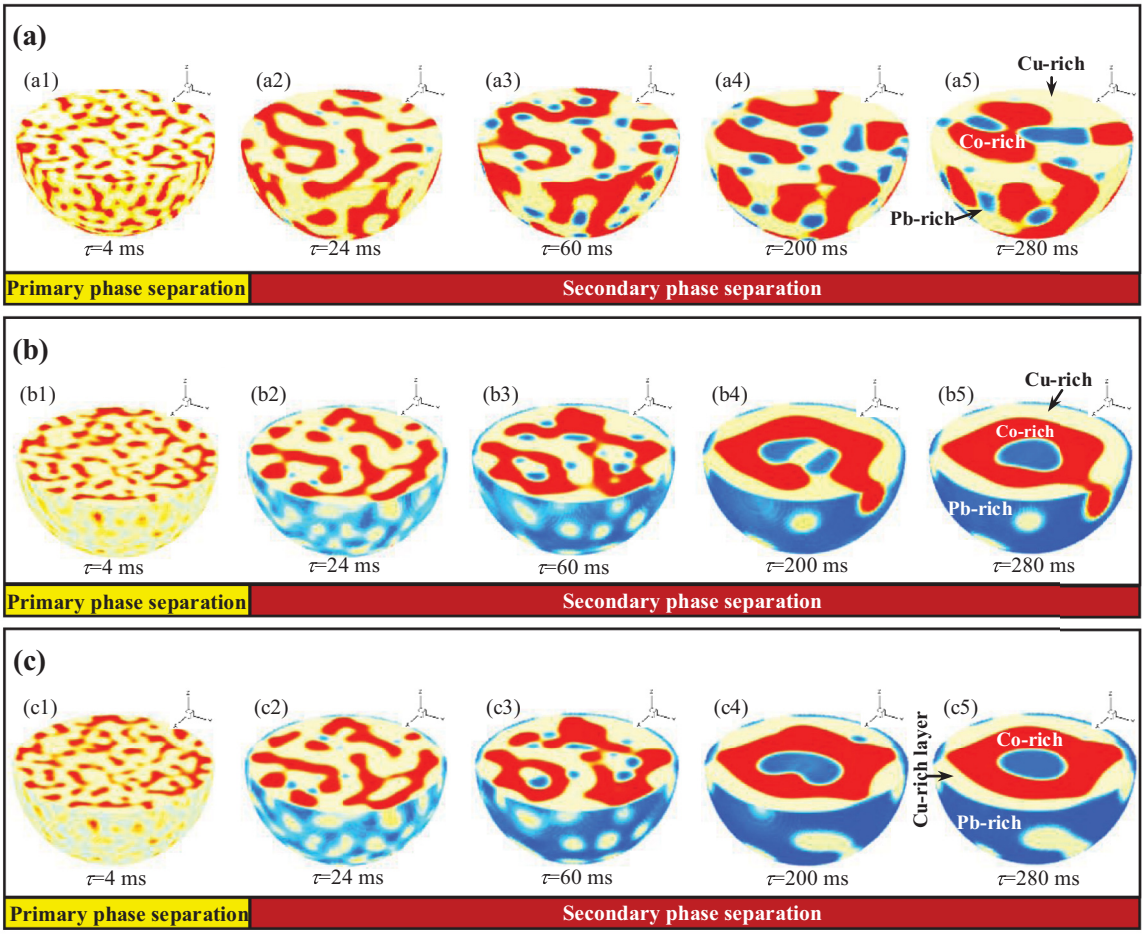

FIG. 5. Three-dimensional phase-separation processes of $Co_{43}Cu_{40}Pb_{17}$ alloy droplets at different conditions: (a) neither surface segregation nor Marangoni convection, (b) with surface segregation but no Marangoni convection, and (c) both surface segregation and Marangoni convection. Here red (dark gray) shows the Co-rich phase, yellow (bright white) shows the Cu-rich phase, and blue (light gray) shows for the Pb-rich phase.

gradient accelerates the growth of the surface segregation shell.

C. Concentration-field evolutions

To explore the formation mechanisms of three-phase three-layer core-shell microstructures in Fig. 1, three parallel simulations of the concentration-field evolutions of Co, Cu, and Pb within $Co_{43}Cu_{40}Pb_{17}$ alloy droplets were performed and the numerical results are shown in Fig. 5. In the first case, assuming that the surface energy differences among Co-, Cu-, and Pb-rich liquid phases are zero and the isothermal field of $0.8T_c$ is imposed in this phase-field model, the three-dimensional phase-separation process of the undercooled $Co_{43}Cu_{40}Pb_{17}$ alloy droplet without Marangoni convection and surface segregation is simulated in Fig. 5(a). Evidently, the homogeneous alloy melt first separates into Co-rich and Cu-rich liquid phases in the form of wormlike structures during the primary PS, as observed in Fig. 5(a1). To decrease the overall interfacial energy between Co-rich and Cu-rich phases, the Co-rich phase can collide, coalesce, and congregate, resulting in a larger wormlike structure in Fig. 5(a2). Meanwhile, the Pb-rich liquid phase starts to separate from the Cu-rich phase in the form of tiny globules. As time evolves, Pb-rich and Cu-rich liquid phases would grow further and finally form a dispersed structure as shown in Fig. 5(a5).

In the second case, the surface segregation is also taken into account in this 3D model and the phase-separation process is reproduced as given in Fig. 5(b). In contrast with the formation process of the dispersed structure in Fig. 5(a5), the Pb-rich phase flows to the droplet surface, forming a Pb-rich shell instead of the random distribution in the first case. This is the reason why the Pb-rich phase always appears at the droplet surface and forms a surface segregation layer, as shown in Fig. 1. It implies that the surface segregation is one of the dynamical mechanisms responsible for the development of the three-phase three-layer core-shell structure.

On the basis of Fig. 5(b), the additional effect of Marangoni convection on the PS is further considered in the model. A nonisothermal temperature field is imposed in such a case. It decreases exponentially along the radial distance from the droplet center to the surface with a total temperature difference of 2 K. The temperature at the surface is set to $0.8T_c$, corresponding to a highly undercooled state. Under this condition, the corresponding structure evolution of the $Co_{43}Cu_{40}Pb_{17}$ droplet is computed in Fig. 5(c). It can be seen

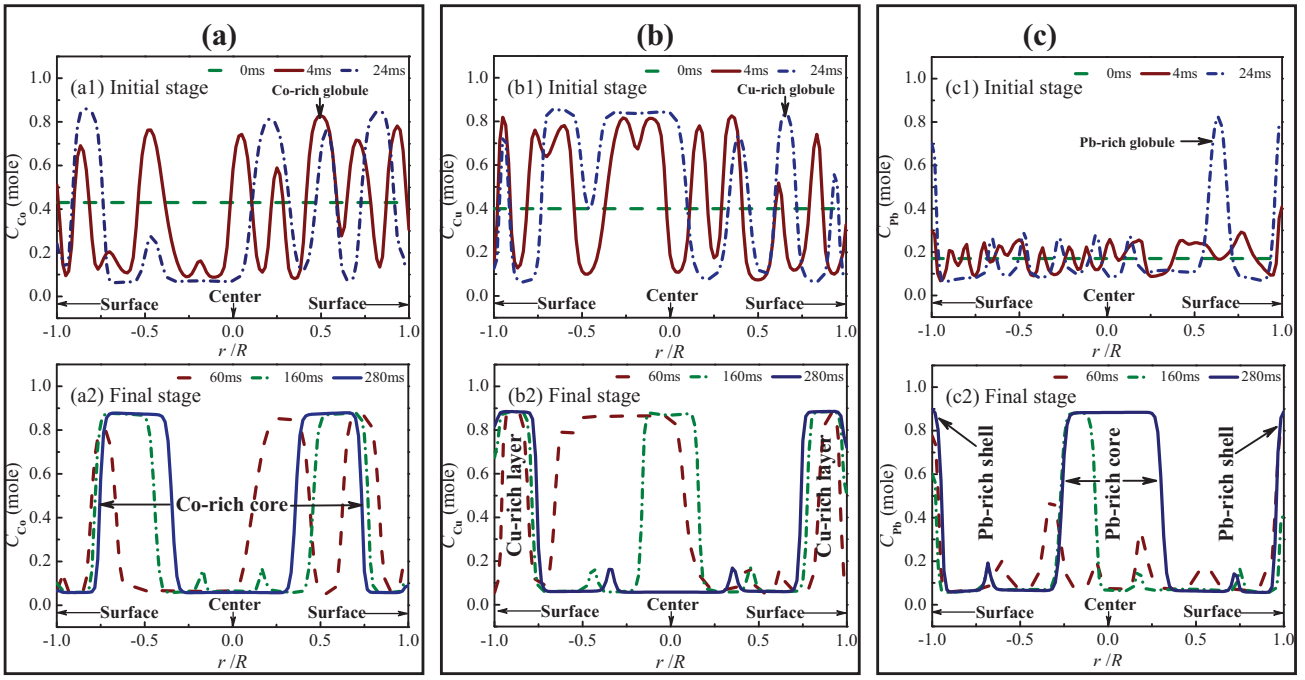

FIG. 6. Concentration curves of solutes and solvent along the radial direction of the $Co_{43}Cu_{40}Pb_{17}$ alloy droplet at various phase-separation moments: (a) solvent Co, (b) solute Cu, and (c) solute Pb.

clearly that the microstructure evolution in this case is more or less the same as that in Fig. 5(b). The only difference is that the separated Co-rich phase during primary PS and Pb-rich phase during secondary PS are forced to migrate to the droplet center owing to the additional Marangoni convection. As a consequence, a three-phase three-layer core-shell structure with a Pb-rich shell, a Cu-rich middle layer, and a Co-rich core forms in the end. The simulated core-shell and dispersed structures are consistent with the experimental observations in Figs. 1 and 3(b). This not only demonstrates the validity of this 3D model in predicting the microstructure evolution, but also reveals that the surface segregation and Marangoni convection are the dynamic mechanisms responsible for the formation of three-phase three-layer core-shell structures. Furthermore, the formation of this structure must satisfy the requirement of a suitable alloy composition that undergoes the primary and then secondary PSs in substantially undercooled liquid states. A short period of phase-separation time facilitates the formation of a dispersed three-phase-separated morphology, whereas a long phase-separation time is required to obtain a three-phase core-shell structure. Though the driving force of phase separation is large enough for small alloy droplets, it allows little time for the aggregation of coexisting liquid phases before the core-shell formation due to their ultrahigh cooling rates. This is the reason why the dispersed three-phase-separated morphologies sometimes form in small alloy droplets, as verified in Fig. 3(b). Accordingly, the formation of these three-phase three-layer core-shell structures can be attributed to the primary PS followed by the coarsening and then secondary PS under the combined effects of surface segregation, Marangoni convection, and phase-separation time.

To further understand the effects of Marangoni convection and surface segregation on the three concentration fields in the process of PS, the concentration curves of Co, Cu, and Pb along the radial direction of the $Co_{43}Cu_{40}Pb_{17}$ alloy droplet at different PS moments are shown in Fig. 6. Apparently, the mole concentrations of both the solvent and solute range from 0 to 1 with the variation of the reduced radius r/R and the coordinates of $(C,0)$ and $(C,\pm 1)$ denote, respectively, the center and surface positions for the Co-Cu-Pb alloy droplet. Before the simulations, the concentration curves of Co, Cu, and Pb remain three constant values. This suggests that the Co-Cu-Pb alloy melt is homogeneous and the liquid PS does not take place at $\tau = 0$ ms. In the initial period of concentration-field evolution, the concentration distribution patterns display drastic fluctuations along the radial direction and then form visible concentration waves, as can be seen in Figs. 6(a1), 6(b1), and 6(c1). With the further continuation of PS, the hydrodynamic effect starts to arise, the Marangoni convection begins to dominate the PS, and the wave peaks of Co concentration are impelled to move toward the droplet center and then aggregate together, forming a Co-rich core at $\tau = 280$ ms, as illustrated in Fig. 6(a2). Meanwhile, the concentration curves of solute Pb and Cu show different evolution characteristics. As PS time increases, the solute concentration of Pb fluctuates more and more intensely and the Pb solute continuously migrates toward the droplet surface due to the surface segregation and forms a conspicuous segregation Pb-rich shell, as observed in Figs. 5(c5) and 6(c2). Although both Cu-rich and Co-rich globules have a tendency to migrate to the droplet center under the effect of Marangoni convection, the center aggregation of these Cu-rich globules cannot occur. Instead, these Cu-rich globules collide and aggregate, forming a Cu-rich layer, which is stuck between the Co-rich core and Pb-rich shell, as shown in Figs. 5(c5) and 6(b2). A possible explanation for the formation of a middle Cu-rich layer is

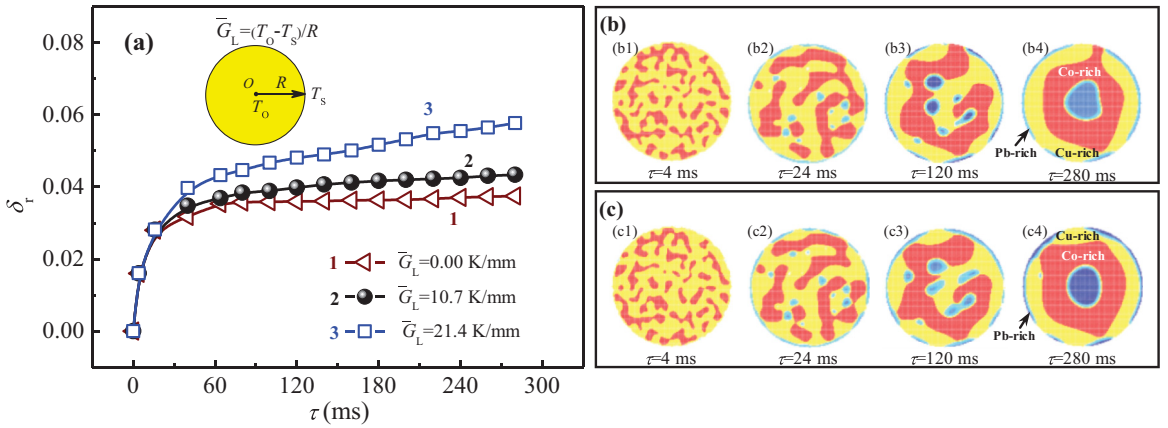

FIG. 7. Effects of droplet temperature gradient on the growth of the Pb-rich shell: (a) reduced thickness δ_r of the Pb-rich shell versus evolution time τ and (b) and (c) cross sections of 3D phase separation at temperature gradients $\bar{G}_L$ of 0 and 21.4 K/mm, respectively.

that the thermal Marangoni migration velocity of Co-rich globules is larger than that of Cu-rich globules owing to the greater temperature coefficient of interfacial energy. In this case, the Co-rich globules are easier to aggregate at the droplet center forming a Co-rich core and the Cu-rich globules have to coagulate together to produce a Cu-rich layer surrounding a Co-rich core.

On the basis of the EDS analyses, the Co content of α (Co), the Cu content of (Cu), and the Pb content of (Pb) are respectively measured as 86, 97, and 77 at. %, whereas the Co content of the Co-rich zone, the Cu content of the Cu-rich zone, and the Pb content of the Pb-rich zone are theoretically predicted as 88.2, 89.1, and 88.5 at. %, respectively. The simulated results basically coincide with those determined by experiments. The discrepancies between experiments and simulations can be ascribed to the estimated interaction energy between different components in Eq. (4) and the model's approximation conditions. Therefore, this 3D phase-field model is a quantitative method and can be used to quantitatively understand the distribution characteristics of both the solvent and solute during phase separation.

As previously analyzed, the alloy droplet diameter is a key parameter that influences the growth of the Pb-rich shell during PS. Because it is computationally expensive to consider other droplets with different sizes, various temperature gradients are taken into account instead to explore the droplet size effect on the growth of the Pb-rich shell. This is equivalent in terms of their effects on the liquid PS within different alloy droplets. Three gradients of 0, 10.7, and 21.4 K/mm were respectively imposed in this 3D phase-field model and the predicted thickness of the Pb-rich shell with the evolution time is statistically measured as shown in Fig. 7(a). With an extension of the evolution time, the Pb-rich shell thickness increases rapidly in the first stage and then slowly increases. As for different temperature gradients, the larger the temperature gradient, the thicker the Pb-rich shell. Numerical results show that the high-temperature gradient contributes to the rapid growth of the Pb-rich shell. The cross-section snapshots of 3D phase separation at temperature gradients of 0 and 21.4 K/mm are simulated, as displayed in Figs. 7(b) and 7(c). Apparently, a larger temperature gradient not only drives the Co-rich globule to aggregate at the droplet center in a shorter period of time, but also facilitates the migration of the Pb solute from inside the droplet to outside and then increases the Pb-rich thickness. In addition, the numerical simulations in Figs. 7(b) and 7(c) still reveal that the greater the temperature gradient, the more drastically the PS proceeds. It can be concluded that the temperature gradient plays an important role in the phase separation and microstructure evolution of Co-Cu-Pb immiscible alloy droplets.

D. Chemical-potential-field variations

In order to explain the evolution mechanisms of concentration fields in Figs. 5(c) and 6, the corresponding chemical-potential-field evolution, which is frequently applied to represent the stability characteristics, should be explored in depth. The chemical-potential evolutions of the solvent Co and solutes Cu and Pb were chosen to analyze their concentration-field evolution and the simulated results are shown in Figs. 8 and 9. At the beginning of PS, the chemical potentials of both the solvent and solute are distributed in a disorderly way, as illustrated in Figs. 8(a1), 8(b1), 8(c1), 9(a1), 9(b1), and 9(c1). The maximum absolute value of solvent Co reaches 4511 J/mol, while those of solutes Cu and Pb attain 3281 and 5429 J/mol, respectively. The disordered distribution patterns and the high chemical potentials at $\tau = 0.0004$ ms indicate that the molten alloy is located in an extreme nonequilibrium state. With the continuation of liquid PS, the distribution pattern of the chemical potential transfers from a disordered state to a relatively ordered state, as shown in Figs. 8(a2)–8(a5), 8(b2)–8(b5), and 8(c2)–8(c5). At the same time, the maximum absolute value of the chemical potential decreases step by step, as illustrated in Fig. 9. This implies that the Gibbs free energy of the $Co_{43}Cu_{40}Pb_{17}$ alloy melt gradually decreases and the system evolves toward a more stable state.

The migration of the solvent Co and solutes Cu and Pb strongly depends on the chemical-potential gradient. Owing to the chemical-potential gradient, the solvent Co and solutes Cu and Pb migrate from the higher-chemical-potential regions to the lower-chemical-potential regions. From Fig. 8 it can be known that the center chemical potential of the solvent Co is less than the droplet periphery over most of the evolution time, whereas that of the solute Pb displays the opposite feature.

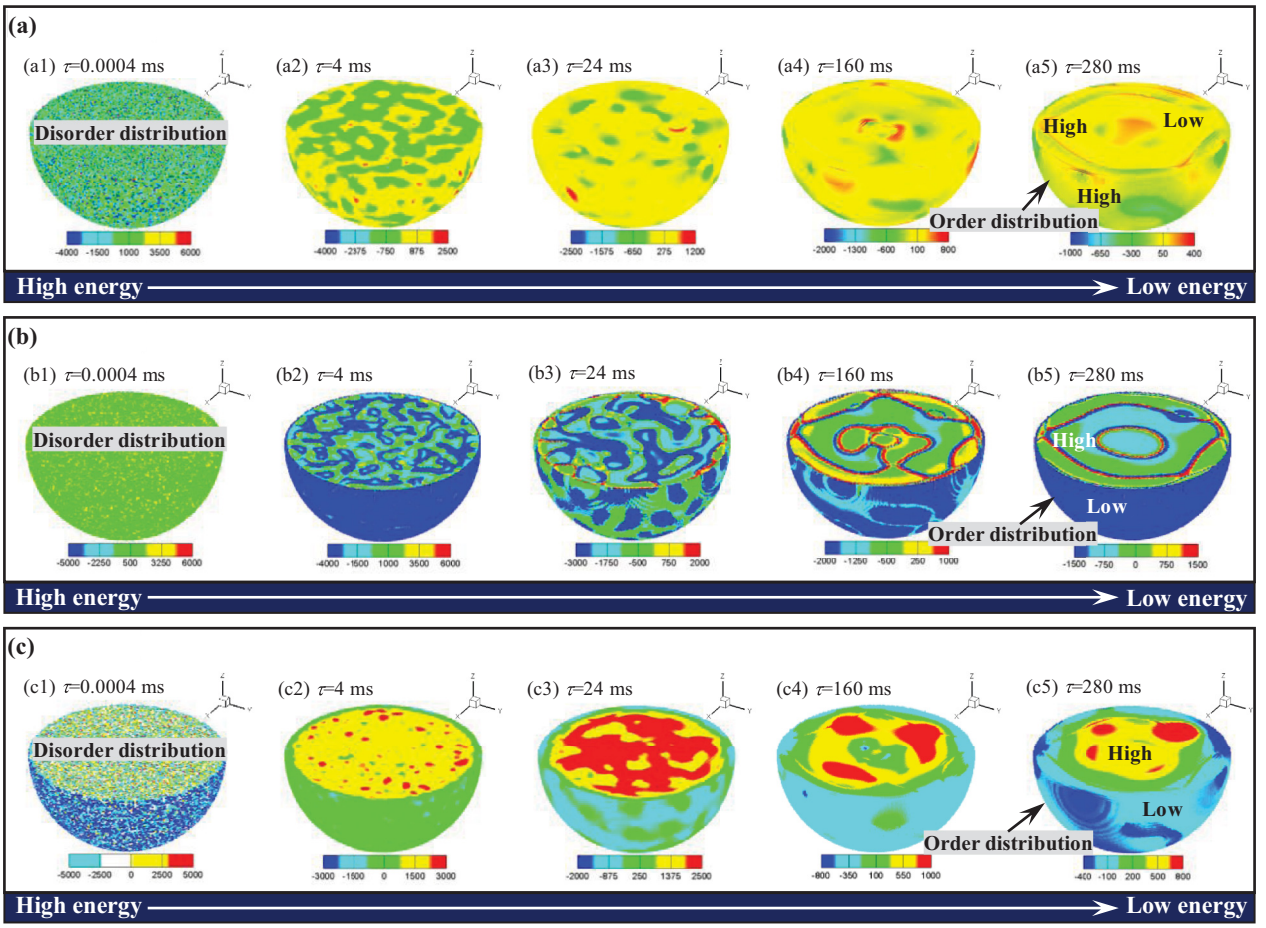

FIG. 8. Three-dimensional chemical-potential evolution of $Co_{43}Cu_{40}Pb_{17}$ alloy droplets: (a) solvent Co, (b) solute Cu, and (c) solute Pb.

In that case, the Co solvent is driven to flow to the droplet center forming a Co-rich core, as exhibited in Figs. 8(a3)–8(a5) and 9(a). In contrast, the Pb solute tends to move to the droplet surface and form a surface segregation shell, as given in Figs. 8(c3)–8(c5) and 9(c). Analogously, the middle zone between the center and peripheral regions of the Co-Cu-Pb droplet has a smaller chemical potential for the Cu-rich phase. This is the reason why the Cu solute mainly occupies the middle zone and finally appears as an intermediate layer. Such migration for Co, Cu, and Pb is conducive to decreasing the system's free energy and subsequently leads to the formation of the phase-separated morphology with a more stable structure. When the PS time lasts 160 ms, a relatively stable three-phase three-layer core-shell microstructure consisting of a Co-rich core, a Cu-rich middle layer, and a Pb-rich shell is formed under the effects of chemical-potential gradients. Therefore, the chemical-potential distribution pattern has an important effect on the fluid dynamics of both the solvent and solute in the process of liquid phase separation.

E. Fluid flow dynamics

To clarify why the Co-rich core is not located at the right center of the core-shell structure, the fluid flow dynamics within these falling alloy droplets should be discussed. As is well known, the final distribution of the Co-rich core is closely linked with the migration mechanisms of Co-rich globules under the reduced-gravity condition. In this case, the movement of the Co-rich globule separated from the parent liquid phase is mainly dominated by the Stokes motion and Marangoni migration. Since the calculation of real-time solutal Marangoni migration is very difficult and it has little effect on the appearance of the eccentric core compared with the effects of Stokes motion and thermal Marangoni migration, the solutal Marangoni convection is not taken into account for simplification. Figure 10(a) shows the velocity sketches of thermal Marangoni migration and Stokes motion for Co-, Cu-, and Pb-rich globules within $Co_{43}Cu_{40}Pb_{17}$ alloy droplets inside the drop tube. Apparently, the variations in the values of the Stokes motion velocity V_S and thermal Marangoni migration velocity V_M with the falling time t play a crucial role in determining the final distribution of Co-, Cu-, and Pb-rich immiscible zones and more attention should be paid to understand the real-time migration of these globules. For this purpose, a theoretical model was proposed to study the real-time migration of small Co-rich globules within a falling $Co_{43}Cu_{40}Pb_{17}$ alloy droplet. The following are the governing equations:

$$(m - m_{\text{gas}})g_0 - 0.5C_r\rho_{\text{gas}}A_c v^2(t) = ma(t), \tag{17}$$

$$a(t)|_{\Delta t\to 0} = \frac{v(t+\Delta t) - v(t)}{\Delta t}, \tag{18}$$

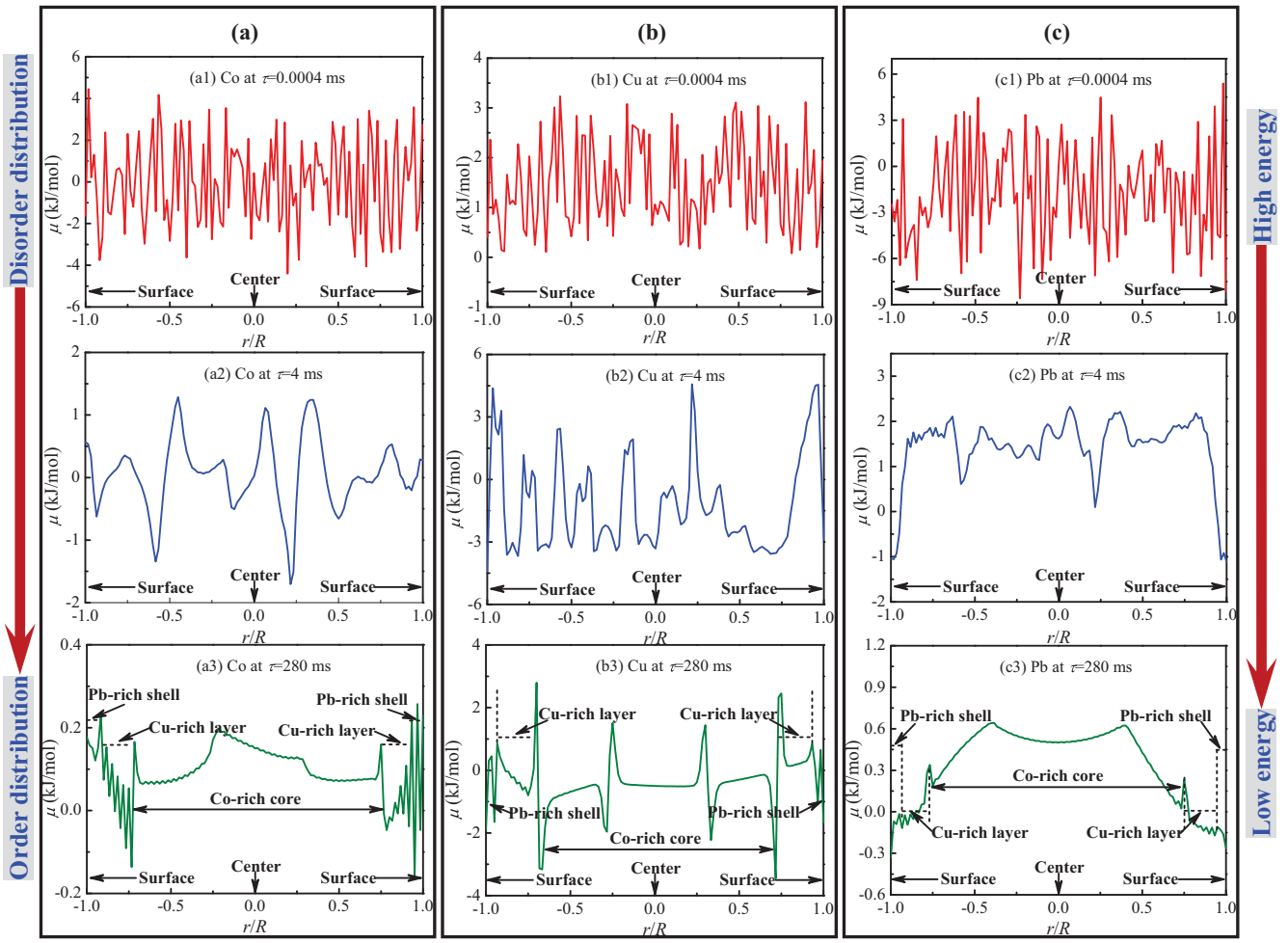

FIG. 9. Chemical-potential curves of solutes and solvent along the radial direction of the $Co_{43}Cu_{40}Pb_{17}$ alloy droplet at different evolution moments: (a) chemical potential of solvent Co, (b) chemical potential of solute Cu, and (c) chemical potential of solute Pb.

$$v(t=0) = V_0, \tag{19}$$

$$V_M = -\frac{2\lambda_1}{(2\lambda_1+\lambda_2)(2\eta_1+3\eta_2)}\frac{\partial\sigma}{\partial T}\frac{\partial T}{\partial r}r_g, \tag{20}$$

$$V_S = \frac{2}{3}\frac{(\rho_2-\rho_1)(\eta_2+\eta_1)}{\eta_1(2\eta_1+3\eta_2)}g' r_g^2. \tag{21}$$

Equations (17)–(19) estimate the droplet gravity level, V_M [34] and V_S [35] are the thermal Marangoni migration velocity and Stokes motion velocity of minor phase globules, respectively, C_r denotes the resistance coefficient, A_c represents the droplet cross-sectional area, g_0 is the gravitational acceleration, $a(t)$ is the droplet accelerated velocity, $v(t)$ is the droplet velocity, V_0 is the droplet initial velocity, r_g is the globule radius of minor phase globules, and g' is the gravity level and is defined as $g_0 - a(t)$. The variation of the temperature field within the alloy droplet can be calculated based on Eqs. (13)–(15). The definitions of other symbols mentioned in Eqs. (17)–(21) can be found elsewhere [34,35]. Because the domain size L increases as $L(t) \sim t^{1/3}$ during the early stage of PS [36], the radius variation $r(t)$ of the Co-rich globule with falling time t could be set as $r_0 t^{1/3}$; r_0 is supposed to be 10 μm in this work. The values of physical parameters used in the calculations were obtained from Ref. [29].

The gravity level of the falling alloy droplet can be computed as a function of falling time, initial velocity, and droplet diameter, as shown in Figs. 11(a) and 11(b). It can be seen that the gravity level gradually increases with the extension of falling time, while the Stokes motion velocity shows an increasing trend in terms of Eq. (21). As displayed in Fig. 4(c), the droplet temperature gradient presents an upward tendency at the initial stage of the fall and then decreases with the further increase in the falling time. It can be deduced that the thermal Marangoni velocity displays a rapid rise at first and subsequently decreases. Thus, a maximum value of V_M/V_S should be observed for every alloy droplet, which has been theoretically demonstrated in Figs. 11(c) and 11(d). In the process of droplet falling, the effect of Stokes motion does not disappear completely. On the contrary, this effect is gradually enhanced once the falling time increases beyond a certain value. The final distribution of Co-, Cu-, and Pb-rich zones can be theoretically predicted according to the speculations of Fig. 10(a). Under the effect of subdued thermal Marangoni migration and enhanced Stokes motion, the center of gravity for Co-rich zones within the Cu-rich zone migrates along the opposite direction of the gravitational field and then moves

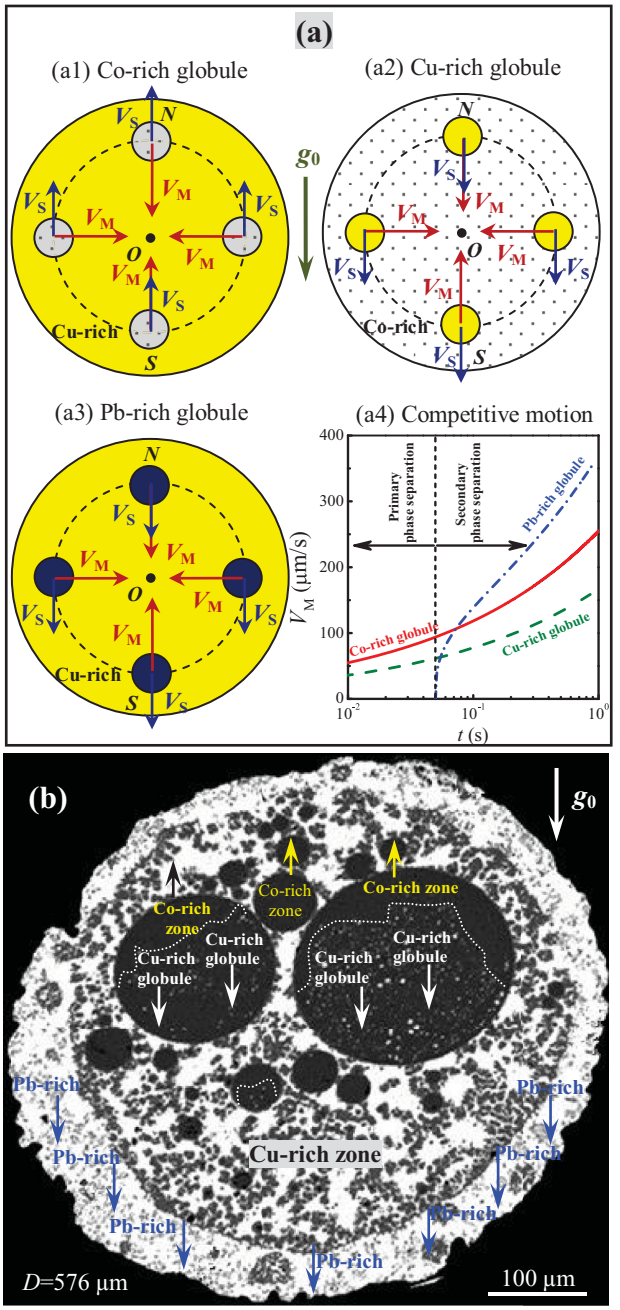

FIG. 10. Theoretical prediction and experimental confirmation of distribution patterns for Co-, Cu-, and Pb-rich globules within $Co_{43}Cu_{40}Pb_{17}$ alloy droplets under microgravity condition: (a) the velocity sketches of thermal Marangoni migration V_M and Stokes motion V_S and (b) experimental evidence.

away from the center of gravity of the Cu-rich zone, as derived in Fig. 10(a1). In contrast, Cu-rich globules inside the Co-rich liquid deviate from the Co-rich zone center along the gravity direction, as depicted in Fig. 10(a2). Analogously, it can be speculated from Fig. 10(a3) that the center of gravity of the Pb-rich zone within the Cu-rich zone is gradually deviating from the Cu-rich zone center and sinks down under normal gravity conditions. Though the Co-rich and Cu-rich globules separated from primary phase separation have a tendency to migrate to the droplet center due to thermal Marangoni convection, the V_M of the Co-rich globule is always larger than that of Cu-rich globules as calculated in Fig. 10(a4) and it is responsible for the formation of the Co-rich core surrounded by a Cu-rich layer. During secondary phase separation, the Pb-rich globules start to separate from the Cu-rich phase and also tend to move to the droplet center. Nevertheless, the Co-rich phase first solidifies because of its highest melting point and this suppresses the center aggregation of Cu-rich and Pb-rich phases. In addition, owing to the smallest surface energy of the Pb-rich phase, it preferentially migrates toward the droplet surface to lower the system's overall energy and a Pb-rich surface segregation layer is formed at the end.

In order to experimentally confirm this prediction, a three-phase multicore-shell structure is presented in Fig. 10(b) to analyze the final distribution patterns of Co-, Cu-, and Pb-rich zones in a reduced-gravity environment. Evidently, Cu-rich tiny globules cannot be observed inside the top regions of Co-rich cores and the closer to the core bottom, the larger the globule size. This indicates that the Cu-rich globules within the Co-rich core migrate along the gravity direction and their center of gravity strays from the core center. Most Co-rich cores are distributed inside the upper regions of the Cu-rich zone, suggesting that the center of gravity of the Co-rich zone deviates from the Cu-rich zone center along the opposite direction of normal gravity. In addition, the Pb-rich liquid shell surrounding a Cu-rich liquid deviates to one side near the center of the earth. The consistency between the theoretical analysis and experimental observation demonstrates that the residual Stokes sedimentation is the main dynamic mechanism responsible for the formation of the eccentric core-shell structure. Sometimes, the temperature field of falling alloy droplets is asymmetrical because of the emissivity difference between the alloy droplet windward and leeward sides, which induces the asymmetrical Marangoni convection and perhaps leads to the formation of an eccentric core. Accordingly, the development of the eccentric core-shell structure can be ascribed to the asymmetric Marangoni convection and the residual Stokes motion.

To understand why the deviation degree of the Co-rich core rises with the decrease of droplet diameter, the ratio β_{MS} of the thermal Marangoni migration velocity and Stokes motion velocity is calculated as a function of initial velocity, droplet diameter, and falling time, as exhibited in Figs. 11(c) and 11(d). Obviously, a larger initial velocity V_0 corresponds to a smaller value of V_M/V_S. This means that the gravity level rises more rapidly for alloy droplets with larger initial velocities. As a consequence, Stokes sedimentation proceeds more intensively at a larger initial velocity and the Co-rich core becomes more and more eccentric. In addition, the gravity level is also related to droplet diameter. As illustrated in Fig. 11(d), the microgravity state disappears more easily for a smaller alloy droplet and the intensity of the Stokes motion is evidently stronger, which probably influences the final distribution of the Co-rich core. Taking into account that the evolution of core-shell microstructures is a time-dependent process, the droplet cooling rate determined by droplet size also influences the formation of the eccentric core. Overall, the deviation degree of the Co-rich core is dominated by the alloy thermodynamics, droplet diameter, and initial velocity. The initial velocities of the droplets are assumed to be the

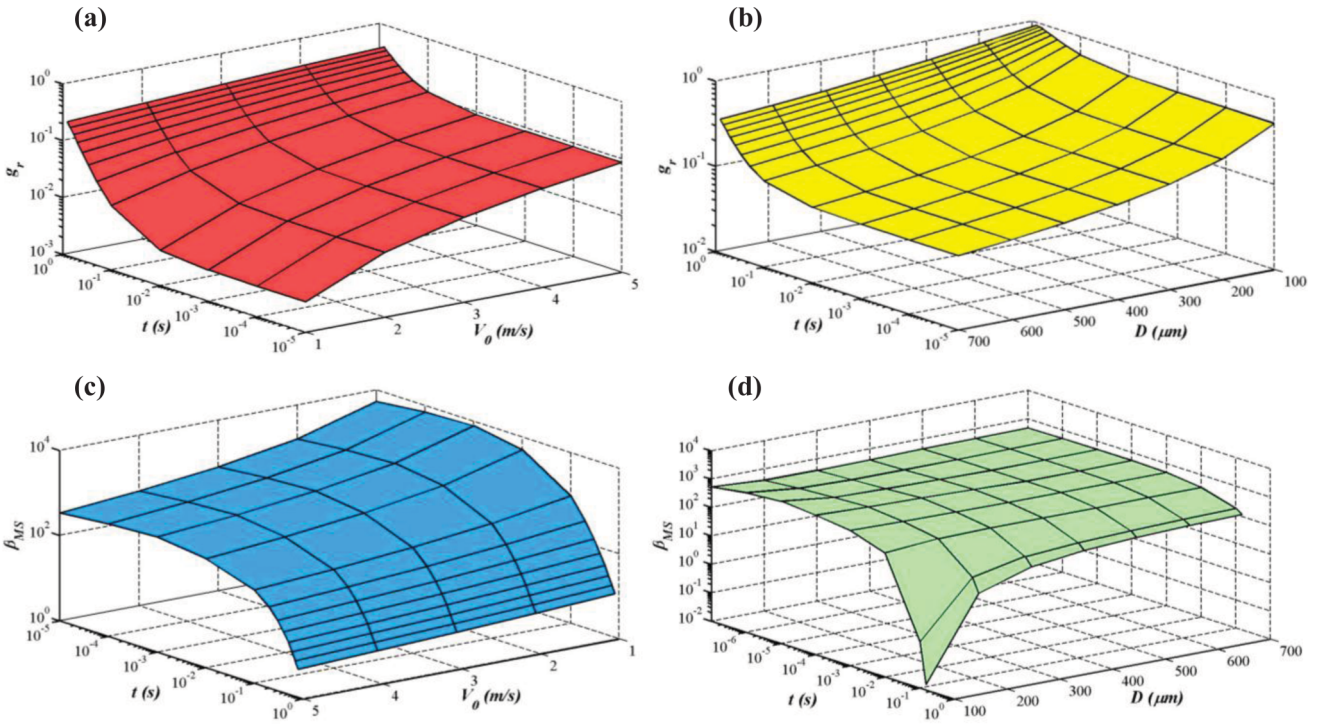

FIG. 11. Migration mechanisms of Co-rich globules within falling droplets of $Co_{43}Cu_{40}Pb_{17}$ alloy versus initial velocity V_0, droplet diameter D, and falling time t: (a) residual gravity g_r-V_0-t at $D = 598\ \mu$m, (b) residual gravity g_r-D-t at $V_0 = 5$ m/s, (c) the ratio β_{MS}-V_0-t of Marangoni migration velocity V_M and Stokes motion velocity V_S at $D = 598\ \mu$m, and (d) β_{MS}-D-t at $V_0 = 5$ m/s.

same in this work. As a smaller alloy droplet generally has a larger undercooling and cooling rate, a shorter migration time is allowed. In such a case, it is difficult for these globules to migrate to the droplet center and form a core structure under the effect of Marangoni convection. In extreme situations, it is possible to preserve a homogeneously dispersed three-phase-separated morphology inside very small alloy droplets due to their ultrahigh undercoolings and cooling rates, as observed in Fig. 3(b). More importantly, the microgravity state of small alloy droplets rapidly vanishes and these globules tend to aggregate together, forming an eccentric core owing to the enhanced effect of Stokes motion. It is the reason why the deviation degree of the Co-rich core is much greater for smaller alloy droplets in Fig. 2(d).

V. CONCLUSION

In summary, a three-phase three-layer core-shell microstructure composed of a Co-rich core, a Cu-rich middle layer, and a Pb-rich shell within an undercooled $Co_{43}Cu_{40}Pb_{17}$ alloy droplet was successfully preserved under the microgravity and containerless conditions inside a drop tube. The droplet size greatly influences the final phase-separated morphology. With a decrease in droplet size, the reduced thickness of the Pb-rich shell displays an increasing trend. In addition, most three-phase three-layer core-shell microstructures processed by the drop tube method exhibit an eccentric Co-rich core and the deviation degree rises with decreasing droplet size. Theoretical analyses revealed that the formation of the eccentric core can be attributed to the residual Stokes sedimentation induced by the reduced-gravity environment and the asymmetric Marangoni convection caused by the emissivity difference between the droplet's windward and leeward sides. Furthermore, the dominant factors that affect the deviation degree have been analyzed in depth. In addition to the three-phase three-layer core-shell structures, several unusual three-phase-separated morphologies such as a multicore shell and a dispersed structure come into being occasionally. The formation of these anomalous phase-separated morphologies can be attributed to the limited phase-separation time for the aggregation of coexisting liquid phases.

A three-dimensional phase-field model was proposed to systematically investigate the dynamic mechanisms of liquid PS for ternary Co-Cu-Pb immiscible alloys. This method takes into account the successive PSs under the combined effect of Marangoni convection and surface segregation. Based on the proposed model, a fundamental understanding of the evolution characteristics of the temperature field, concentration field, and chemical-potential field has been developed. The numerical simulations show that the evolution of three-phase three-layer core-shell structures must satisfy the requirement of suitable alloy composition that undergoes two successive PSs in a highly undercooled state. The formation of this three-phase three-layer core-shell structure can be ascribed to the primary and then the secondary PSs under the combined effect of Marangoni convection and surface segregation. The simulated core-shell and dispersed microstructures are in accord with the experimental observations, which verify the validity of the proposed phase-field model in predicting the phase separation and microstructure evolution of ternary immiscible alloys. Due to the Marangoni convection, the Co-rich phase is preferentially impelled to migrate to the droplet center with

a smaller chemical potential, which contributes significantly to the development of the Co-rich core. In contrast, the Pb-rich phase with the smallest surface energy tends to continuously flow to the droplet surface with a reduced chemical potential and forms a conspicuous segregation shell under the effect of surface segregation. Since a smaller alloy droplet possesses a larger temperature gradient, the chemical-potential gradient between the droplet center and surface increases considerably. As a consequence, Co-rich globules inside a smaller alloy droplet migrate to the droplet center and the Pb-rich phase flows to the droplet surface in a shorter period of time. This is conducive to increasing the reduced thickness of the surface segregation shell. The simulation results not only provide a deep understanding of multiphase core-shell structures, but also shed some light on utilizing liquid phase-separation processes to synthesize more complicated core-shell structures for potential applications.

ACKNOWLEDGMENTS

The authors are very grateful to Dr. J. Chang, S. J. Yang, and X. P. Qin for their help with the experiments and simulations. This work was financially supported by the National Natural Science Foundation of China (Grants No. 51271150, No. 51371150, No. 51571163, No. 51327901, and No. 51301138).

[1] P. Varytis, P. A. Pantazopoulos, and N. Stefanou, Enhanced Faraday rotation by crystals of core-shell magnetoplasmonic nanoparticles, Phys. Rev. B **93**, 214423 (2016).

[2] A. Slimani, K. Boukheddaden, and K. Yamashita, Thermal spin transition of circularly shaped nanoparticles in a core-shell structure investigated with an electroelastic model, Phys. Rev. B **89**, 214109 (2014).

[3] W. L. Wang, Y. H. Wu, L. H. Li, D. L. Geng, and B. Wei, Dynamic evolution process of multilayer core-shell microstructures within containerlessly solidifying $Fe_{50}Sn_{50}$ immiscible alloy, Phys. Rev. E **93**, 032603 (2016).

[4] L. B. Skinner, C. J. Benmore, J. K. R. Weber, J. Du, J. Neuefeind, S. K. Tumber, and J. B. Parise, Low Cation Coordination in Oxide Melts, Phys. Rev. Lett. **112**, 157801 (2014).

[5] W. Tang, Y. Q. Wu, K. W. Dennis, N. T. Oster, M. J. Kramer, I. E. Anderson, and R. W. McCallum, Magnetic properties and microstructure of gas atomized $MRE_2(Fe,Co)_{14}B$ powder with ZrC addition (MRE = Nd + Y + Dy), J. Appl. Phys. **105**, 07A728 (2009).

[6] S. Shklyaev, A. A. Alabuzhev, and M. Khenner, Marangoni convection in a thin film on a vertically oscillating plate, Phys. Rev. E **92**, 013019 (2015).

[7] M. Hoell, H. Kantz, and Y. Zhou, Detrended fluctuation analysis and the difference between external drifts and intrinsic diffusionlike nonstationarity, Phys. Rev. E **94**, 042201 (2016).

[8] D. Zwicker, A. A. Hyman, and F. Jülicher, Suppression of Ostwald ripening in active emulsions, Phys. Rev. E **92**, 012317 (2015).

[9] Z. G. Sun, W. Löser, J. Eckert, K.-H. Müller, and L. Schultz, Phase separation in $Nd_{60-x}Y_xFe_{30}Al_{10}$ melt-spun ribbons, Appl. Phys. Lett. **80**, 772 (2002).

[10] H. L. Li and J. Z. Zhao, Convective effect on the microstructure evolution during a liquid-liquid decomposition, Appl. Phys. Lett. **92**, 241902 (2008).

[11] W. Chen, A. S. Foster, M. J. Alava, and L. Laurson, Stick-Slip Control in Nanoscale Boundary Lubrication by Surface Wettability, Phys. Rev. Lett. **114**, 095502 (2015).

[12] I. Thompson, F. Duan, and C. A. Ward, Absence of Marangoni convection at Marangoni numbers above 27,000 during water evaporation, Phys. Rev. E **80**, 056308 (2009).

[13] Y. H. Wu, W. L. Wang, Z. C. Xia, and B. Wei, Phase separation and microstructure evolution of ternary Fe-Sn-Ge immiscible alloy under microgravity condition, Comput. Mater. Sci. **103**, 179 (2015).

[14] J. Z. Zhao, Formation of the minor phase shell on the surface of hypermonotectic alloy powders, Scripta Mater. **54**, 247 (2006).

[15] N. Yan, W. L. Wang, and B. Wei, Complex phase separation of ternary Co-Cu-Pb alloy under containerless processing condition, J. Alloy. Compd. **558**, 109 (2013).

[16] J. J. Si, T. Wang, Y. D. Wu, Y. H. Cai, X. H. Chen, W. Y. Wang, Z. K. Liu, and X. D. Hui, Cr-based bulk metallic glasses with ultrahigh hardness, Appl. Phys. Lett. **106**, 251905 (2015).

[17] W. M. Jacobs, D. W. Oxtoby, and D. Frenkel, Phase separation in solutions with specific and nonspecific interactions, J. Chem. Phys. **140**, 204109 (2014).

[18] R. Krishnan, P. K. Jaiswal, and S. Puri, Phase separation in antisymmetric films: A molecular dynamics study, J. Chem. Phys. **139**, 174705 (2013).

[19] N. A. Mahynski and A. Z. Panagiotopoulos, Phase behavior of athermal colloid-star polymer mixtures, J. Chem. Phys. **139**, 024907 (2013).

[20] Y. H. Wu, W. L. Wang, and B. Wei, Predicting and confirming the solidification kinetics for liquid peritectic alloys with large positive mixing enthalpy, Mater. Lett. **180**, 77 (2016).

[21] C. Tung and A. Cacciuto, Phase separation of mixed polymer brushes on surfaces with nonuniform curvature, J. Chem. Phys. **139**, 194902 (2013).

[22] N. Vladimirova, S. Derevyanko, and G. Falkovich, Phase transitions in wave turbulence, Phys. Rev. E **85**, 010101(R) (2012).

[23] A. Krekhov, Formation of regular structures in the process of phase separation, Phys. Rev. E **79**, 035302(R) (2009).

[24] N. Vladimirova, A. Malagoli, and R. Mauri, Two-dimensional model of phase segregation in liquid binary mixtures, Phys. Rev. E **60**, 6968 (1999).

[25] G. I. Tóth, Phase-field modeling of isothermal quasi-incompressible multicomponent liquids, Phys. Rev. E **94**, 033114 (2016)

[26] G. I. Tóth, M. Zarifi, and B. Kvamme, Phase-field theory of multicomponent incompressible Cahn-Hilliard liquids, Phys. Rev. E **93**, 013126 (2016).

[27] J. H. Hildebrand and R. L. Scott, *Regular Solution* (Prentice Hall, Englewood Cliffs, 1962).

[28] D. A. Porter and K. E. Easterling, *Phase Transformation in Metals and Alloys* (Van Nostrand Reinhold, London, 1981).

[29] J. W. Cahn and J. E. Hilliard, Free energy of a nonuniform system. I. Interfacial free energy, J. Chem. Phys. **28**, 258 (1958).

[30] P. C. Hohenberg and B. I. Halperin, Theory of dynamic critical phenomena, Rev. Mod. Phys. **49**, 435 (1977).

[31] N. M. Maurits, A. V. Zvelindovsky, G. J. A. Sevink, B. A. C. van Vlimmeren, and J. G. E. M. Fraaije, Hydrodynamic effects in three-dimensional microphase separation of block copolymers: Dynamic mean-field density functional approach, J. Chem. Phys. **108**, 9150 (1998).

[32] C. J. Smithells, *Metals Reference Book*, 6th ed. (Butterworth, London, 1984).

[33] Z. Q. Li, W. L. Wang, W. Zhai, and B. Wei, Formation mechanism of layered microstructure and monotectic cell within rapidly solidified $Fe_{62.1}Sn_{27.9}Si_{10}$ alloy, Acta Phys. Sin. **60**, 108101 (2011).

[34] N. O. Young, J. S. Goldstein, and M. J. Block, The motion of bubbles in a vertical temperature gradient, J. Fluid Mech. **6**, 350 (1959).

[35] J. R. Rogers and R. H. Davis, Modeling of collision and coalescence of droplets during microgravity processing of Zn-Bi immiscible alloys, Metall. Mater. Trans. A **21**, 59 (1990).

[36] A. E. Bailey, W. C. K. Poon, R. J. Christianson, A. B. Schofield, U. Gasser, V. Prasad, S. Manley, P. N. Segre, L. Cipelletti, W. V. Meyer, M. P. Doherty, S. Sankaran, A. L. Jankovsky, W. L. Shiley, J. P. Bowen, J. C. Eggers, C. Kurta, T. Lorik, Jr., P. N. Pusey, and D. A. Weitz, Spinodal Decomposition in a Model Colloid-Polymer Mixture in Microgravity, Phys. Rev. Lett. **99**, 205701 (2007).